

X-ray Measurement of Dark Matter “Temperature” in Abell 1795

Yasushi Ikebe¹

*Joint Center for Astrophysics, University of Maryland, Baltimore County, 1000 Hilltop
Circle, Baltimore, MD 21250, USA*

ikebe@milkyway.gsfc.nasa.gov

Hans Böhringer

*Max-Planck-Institut für extraterrestrische Physik, Postfach 1312, 85741 Garching,
Germany*

and

Tetsu Kitayama

Department of Physics, Toho University, Miyama, Funabashi, Chiba 274-8510, Japan

ABSTRACT

We present a method from an X-ray observation of a galaxy cluster to measure the radial profile of the dark matter velocity dispersion, σ_{DM} , and to compare the dark matter “temperature” defined as $\mu m_{\text{p}} \sigma_{\text{DM}}^2 / k_{\text{B}}$ with the gas temperature. The method is applied to the XMM-Newton observation of Abell 1795. The ratio between the specific energy of the dark matter and that of the intracluster medium (ICM), which can be defined as β_{DM} in analogy with β_{spec} , is found to be less than unity everywhere ranging $\sim 0.3 - 0.8$. In other words, the ICM temperature is higher than the dark matter “temperature”, even in the central region where the radiative cooling time is short. A β_{DM} value smaller than unity can most naturally be explained by heating of the ICM. The excess energy of ICM is estimated to be $\sim 1 - 3$ keV per particle.

Subject headings: dark matter — X-rays: galaxies: clusters

¹Office address: Code 661, NASA/Goddard Space Flight Center, Greenbelt Rd., Greenbelt, MD 20771, USA

1. Introduction

Early X-ray imaging observations with the *Einstein* observatory and *ROSAT* showed that in the central regions of clusters of galaxies the radiative cooling time is shorter than the age of the universe (e.g. Canizares, Stewart, & Fabian 1983). As a result, the intra-cluster medium (ICM) should cool down to form a cold ($T < 10^6\text{K}$) gas phase inducing a global inflow of gas. This “cooling flow” (see Fabian 1994 for a review) picture has been extensively discussed and formed a basic assumption in many arguments. The low resolution spectroscopy in 0.5-2 keV by *ROSAT* showed that in some clusters the ICM temperature actually decreases towards the center (e.g. Böhringer et al. 1994; David et al. 1994; Allen & Fabian 1994). Higher resolution spectroscopy in 0.5-10 keV with *ASCA*, however, can not be fully understood with the conventional cooling flow model. *ASCA* spectra of cooling flow clusters can be well explained by a two (hot and cool) phase plasma without significant excess absorption features (e.g. Ikebe et al. 1999; Makishima et al. 2001). A naive cooling flow model predicting a range of temperatures with intrinsic absorption could also fit the *ASCA* data but generally produce worse chi-square results (e.g. Allen et al. 2001). Most recently, very high resolution spectroscopy with XMM-Newton/RGS unambiguously show that there is very little X-ray emission from gas cooler than certain lower cut-off temperatures of $\sim 1 - 3$ keV (Tamura et al. 2001; Kaastra et al. 2001; Peterson et al. 2001). Unless a large amount of cooled gas or the metals in the cold gas are hidden (Fabian et al. 2001a), there must exist a heating mechanism that prevents the ICM from radiative cooling.

The necessity of global heat input into the ICM in addition to gravitational heating has also been pointed out from the break of the self-similarity between dark matter and ICM, which is most clearly demonstrated in the X-ray luminosity-temperature relation ($L - T$ relation). A simple scaling analysis (Kaiser 1986) suggests a relation of $L \propto T^2$, while observation shows $L \propto T^3$ (e.g. Edge & Stewart 1991; David et al. 1993; White et al. 1997; Wu et al. 1999). The break of the self-similarity is also seen in the entropy vs temperature relation. Ponman, Cannon, & Navarro (1999) showed that cooler systems ($T < 4$ keV) have entropies higher than achievable through gravitational collapse alone. Simulation studies show that the observed relations can be reproduced, if there is enough non-gravitational heat input into the ICM by feedback from galaxies (e.g. Metzler & Evrard 1994; Bower et al. 2001) or preheating before the cluster formation (e.g. Navarro et al. 1995; Tozzi & Norman 2000).

In order to shed some new light onto these “cooling flow phenomena” and “break of self similarity”, we, in the present paper, perform a comparison of the temperature distribution of the ICM to the distribution of the velocity dispersion of the dark matter. A parameter, $\beta_{\text{spec}} \equiv \sigma_{\text{gal}}^2 / (k_{\text{B}}T / \mu m_p)$, is often used as a measure of the average kinetic energy per unit

mass in galaxies relative to that in the ICM. From observations of many clusters, the mean β_{spec} is ~ 1 with large scatter (e.g. Wu et al. 1999), indicating that the energy equipartition between galaxies and ICM is roughly achieved on average. In analogy with β_{spec} , we can introduce $\beta_{\text{DM}} \equiv \sigma_{\text{DM}}^2 / (k_{\text{B}}T / \mu m_{\text{p}})$ for comparison between the mean kinetic energy of the dark matter and that of the ICM, and define the dark matter “temperature” as $T_{\text{DM}} \equiv \mu m_{\text{p}} \sigma_{\text{DM}}^2 / k_{\text{B}}$. Note that the above definition of “temperature”, by means of proton mass instead of the actual mass of dark matter particles, is only for the sake of comparison with the gas temperature. Therefore we put “temperature” in quotes. We obtain, in this paper, the radial profile of the β_{DM} value observationally for the first time.

In Sect. 2, we describe the method of measuring the dark matter velocity dispersion in a cluster of galaxies from an X-ray observation. We applied the method to the XMM-Newton data of a prototypical cooling flow cluster, Abell 1795 (hereafter A1795), which is located at $z=0.0616$ (Struble & Rood 1987). The X-ray data analysis and results are presented in Sect. 3. Discussion and summary are found in Sect. 4 and Sect. 5, respectively. Throughout the paper, the Hubble constant is given as $70 h_{70} \text{ km s}^{-1} \text{ Mpc}^{-1}$, and a flat universe ($\Omega_{\text{m},0} = 0.3$, $\Omega_{\Lambda,0} = 0.7$) is assumed. At the redshift of A1795, 1 arcsec corresponds to 1.19 kpc.

2. Method of measuring dark matter velocity dispersion

We use a simplified model cluster being composed of a hot plasma ICM with a temperature of $10^7 - 10^8$ K, and dark matter made of collisionless particles. Under the assumptions of spherical symmetry and hydrostatic equilibrium, the ICM distribution is described by

$$\frac{GM}{R} = -\frac{k_{\text{B}}T_{\text{g}}}{\mu m_{\text{p}}} \left(\frac{d \ln n_{\text{g}}}{d \ln R} + \frac{d \ln T_{\text{g}}}{d \ln R} \right), \quad (1)$$

where $M(< R)$ is the total gravitating mass within a sphere of radius R , k_{B} is the Boltzmann constant, G is the Gravitational constant, $n_{\text{g}}(R)$ and $T_{\text{g}}(R)$ is the density and temperature of the ICM, respectively. From an X-ray observation, $n_{\text{g}}(R)$ and $T_{\text{g}}(R)$ are measured and $M(< R)$ can be obtained via Eq. (1). When the dark matter particles tracing the same gravitational field are in steady state, they obey the Jeans equation

$$\frac{GM}{R} = -\sigma_{\text{DM}}^2 \left(\frac{d \ln \rho_{\text{DM}}}{d \ln R} + \frac{d \ln \sigma_{\text{DM}}^2}{d \ln R} \right), \quad (2)$$

where $\sigma_{\text{DM}}(R)$ is the one-dimensional radial velocity dispersion, and ρ_{DM} is the mass density, which is given as $\rho_{\text{DM}} = \frac{1}{4\pi R^2} \frac{dM}{dR} - \mu m_{\text{p}} n_{\text{g}}$. Therefore, once the total gravitating mass, M , and the gas density, n_{g} , profiles are obtained from an X-ray observation, Eq. (2) contains

only one unknown parameter, $\sigma_{\text{DM}}(R)$. Equation (2) can be rewritten in the form of an ordinary differential equation for σ_{DM}^2 as

$$\frac{d\sigma_{\text{DM}}^2}{dR} = -\frac{GM}{R^2} - \frac{\sigma_{\text{DM}}^2}{\rho_{\text{DM}}} \frac{d\rho_{\text{DM}}}{dR}, \quad (3)$$

which can be solved numerically under a given boundary condition to derive the velocity dispersion profile of the dark matter.

Although a steady state dark matter distribution is assumed above, a dark matter density profile should actually be growing as matter is falling onto the system from outside. A numerical simulation by Fukushige & Makino (2001) shows that the dark matter halo grows in a self-similar way, keeping the density profile in the central region unchanged. This justifies the assumption at least in the central region.

A similar technique as described above was used in determining the ICM temperature profile, using X-ray imaging data without spectroscopic information taken e.g. with the *Einstein* observatory. A model profile for the total mass is assumed and the temperature profile is derived from the equation of hydrostatic equilibrium so that the observed brightness profile is explained (e.g. Fabian et al. 1981; Hughes 1989). Here we solve the Jeans equation instead in order to derive the dark matter velocity dispersion.

3. A1795 and the XMM-Newton observation

An ideal opportunity to study the mass profile as well as velocity dispersion profile of dark matter is provided by the XMM-Newton observation of a prototypical cooling flow cluster, A1795. Early X-ray imaging observations with the *Einstein* observatory and *ROSAT* showed that the X-ray emission from A1795 has almost circular symmetry with a small elongation along the north-south direction, which indicates that the cluster is well relaxed dynamically (Jones & Forman 1984; Boute & Tsai 1996). The radial brightness profile shows a huge central excess above a prediction from an isothermal β -model profile, and the central excess luminosity gives a mass deposition rate of $\sim 250h_{70}^{-2} M_{\odot} \text{ yr}^{-1}$ based on the standard cooling flow interpretation (Edge et al. 1992; Briel & Henry 1996). From the 0.5-10 keV spectrum taken with *ASCA*, however, a significantly smaller mass deposition rate is obtained ($\sim 66h_{70}^{-2} M_{\odot} \text{ yr}^{-1}$ Fabian et al. 1994; $\sim 70h_{70}^{-2} M_{\odot} \text{ yr}^{-1}$ Xu et al. 1998; $\sim 150h_{70}^{-2} M_{\odot} \text{ yr}^{-1}$ Allen et al. 2001). Instead of the cooling flow model, the *ASCA* spectrum can be best described with a two temperature model without excess absorption (Xu et al. 1998).

The XMM-Newton observation of A1795 was carried out during the performance-verification phase on June 26 2000 with total observing time of ~ 50 ksec. The ICM temperature pro-

file obtained with EPIC MOS as well as EPIC PN were already reported by Tamura et al. (2001) and by Arnaud et al. (2001), showing that it is almost isothermal at ~ 6 keV in the 2-10 arcmin radius region, while it decreases towards the center reaching the minimum temperature at ~ 3 keV. The Chandra observation gives consistent results (Ettori et al. 2002). A high resolution spectrum from the central region obtained with XMM-Newton/RGS has been analyzed by Tamura et al. (2001), showing a lack of signature of cool gas components below ~ 3 keV and an upper limit of $77 h_{70}^{-2} M_{\odot} \text{ yr}^{-1}$ for the mass deposition rate is obtained if an isobaric cooling flow model is applied.

In this paper, we analyze the data taken with the XMM-Newton/EPIC PN, MOS1 and MOS2 to measure the total mass profile of A1795 and to derive the dark matter velocity dispersion profile using the method described in Sect. 2.

4. Analysis of the XMM-Newton data and results

4.1. Data screening and background subtraction

A significant fraction of any XMM-Newton observation is often contaminated by the huge background count rate by soft proton flares. In order to derive time intervals with stable background, we made the 0.5–10 keV band lightcurves individually with the PN, MOS1, and MOS2 data, and eliminated time periods where the count rate deviates from the mean value during quiescent periods by $\geq 2\sigma$. The total usable exposure time thus left is 23 ksec, 31 ksec, and 34 ksec for PN, MOS 1 and MOS 2, respectively. In the present analysis, the single and double pixel events of the PN data and the single, double, triple, and quadruple events of the MOS data are used.

The background consisting of the cosmic X-ray background and the high energy particle events was estimated from the Lockman Hole data taken during the revolution # 70. In this sky region, the Galactic column density is as low as the A1795 field. After eliminating the contamination sources from the Lockman Hole data as well as the A1795 data, the Lockman Hole data are scaled so that the count rates of the background and the cluster data becomes the same in the 7-12 keV energy band, and in the radius range of 575-925 arcsec for PN and of 500-850 arcsec for MOS, where no significant X-ray signal from the cluster was detected. The background data thus obtained were subtracted from the cluster data. For PN, the out-of-time events (Strüder et al. 2001) were also subtracted prior to the subtraction of the background.

4.2. Radial count rate profile

Defining the center as the X-ray peak position, we have produced a projected radial brightness profile in the 0.8-10 keV band. The X-ray count rate was converted to the X-ray flux by correcting each X-ray photon with the instruments' responses that include the effective area and vignetting of the X-ray telescopes, and the quantum efficiency of the CCD cameras. Combining the data taken with PN, MOS1 and MOS2, we thus derived the brightness profile, which is illustrated in Fig. 1. For comparison with the other X-ray observations, we quantified the radial profile using the β -model profile given by

$$\Sigma = \Sigma_0 \left[1 + \left(\frac{R}{R_c} \right)^2 \right]^{-3\beta+0.5}, \quad (4)$$

where R_c is a core radius and β is a beta parameter. The β model has been often used to fit X-ray brightness profiles and generally gives a good representation for non cooling flow clusters. Since the X-ray brightness profile of A1795 has long been known to show a central excess above a β -model profile, we employed here a double β -model profile that is the sum of two β -model profiles to fit the 0.8-10 keV brightness profile within 848 arcsec. In the actual fitting, the model brightness profile is convolved with the point spread function of the X-ray telescope ¹, whose half-power-radius is ~ 9 arcsec at 1.5 keV on-axis and significantly affects several of the central bins. Evaluating the goodness of the fit with a chi-square statistic, we obtained a good fit as shown in Fig. 1 with the best-fit parameters as summarized in table 1.

4.3. ICM temperature and metallicity profile

The temperature and metallicity profiles given by Tamura et al. (2001) were derived from the conventional annular spectral analysis, accumulating spectra from concentric annular regions in the projected 2-dimensional space. We derive here the temperature and metallicity profiles instead in 3-dimensional form from deprojected spectra. With each PN,

¹The PSF is approximated by an analytic function given as $\left[1 + \left(\frac{r}{r_c} \right)^2 \right]^{-\alpha}$, where r_c and α depend on off-axis angle as well as X-ray energy (see Ghizzardi 2001). We assumed that the PSF is constant in the entire FOV and independent of the X-ray energy. As the representative, we employed the on-axis PSF at 1.5 keV. Using the r_c and α parameters of $(r_c[\text{arcsec}], \alpha) = (5.37, 1.5)$, $(4.72, 1.457)$, and $(4.4545, 1.4035)$, for PN, MOS1, and MOS2, respectively, we obtained the average PSF, which is then used in the brightness profile fittings.

MOS1, and MOS2 data set, we first accumulate 13 annular spectra from the vignetting corrected count rate profiles in individual energy channels. The outer radii are 16, 32, 48, 64, 96, 128, 192, 256, 384, 512, 640, 768, and 848 arcsec. Assuming spherical symmetry and that there is no cluster emission beyond 848 arcsec from the cluster center, we deprojected the annular spectra to spectra for 13 spherical shell regions whose radii correspond to the annular radii. Since no intrinsic absorption is found even from the central region (Tamura et al. 2001), the X-ray emission from the cluster is entirely optically thin, and we performed the deprojection process as follows. The relation between the energy spectra observed in the N annular regions, $S_j(E)$ ($j = 1 - N$), and those emitted from the N shell regions, $C_i(E)$ ($i = 1 - N$), is given with a matrix relation as

$$S_j(E) = \sum_{i=1}^N M_{j,i} C_i(E) , \quad (5)$$

where $N = 13$ in the present case. The matrix elements are given as

$$M_{j,i} = \begin{cases} [(r_{i+1}^2 - r_j^2)^{3/2} - (r_i^2 - r_j^2)^{3/2} - (r_{i+1}^2 - r_{j+1}^2)^{3/2} + (r_i^2 - r_{j+1}^2)^{3/2}] / (r_{i+1}^3 - r_i^3) & \text{if } i > j, \\ (r_{i+1}^2 - r_i^2)^{3/2} / (r_{i+1}^3 - r_i^3) & \text{if } i = j, \\ 0 & \text{if } i < j, \end{cases} \quad (6)$$

where r_i (r_j) and r_{i+1} (r_{j+1}) are the inner and the outer radius of the i 'th shell (j 'th annular), respectively. Each element represents the volume fraction of the i 'th shell contributing to the emission detected in the j 'th annular. Since $M_{j,i}$ is a triangular matrix, it can be easily inverted to $M_{i,j}^{-1}$, and the deprojected shell region spectra can be derived from the annular spectra by

$$C_i(E) = \sum_{j=1}^N M_{i,j}^{-1} S_j(E) . \quad (7)$$

Statistical errors in the individual energy bins are properly propagated through this operation.

Out of the 13 deprojected spectra thus derived from each PN, MOS1, and MOS2 data set, we used only the inner 10 deprojected spectra within a 512 arcsec radius in the analysis below so that the artificial cut-off of the X-ray emission outside the maximum radius of 848 arcsec does not affect the resulting deprojected spectra within 512 arcsec. In addition, the signal to noise ratios of the spectra within 512 arcsec are high enough, and some 10% systematic error of the predicted background count rates introduce no significant systematic errors on temperature measurements.

In order to derive the temperature and metallicity profile, we simultaneously fitted the PN, MOS1, and MOS2 spectra with a single-temperature plasma model in each deprojected

shell region. We employed the MEKAL model (Mewe et al. 1985, 1986; Kaastra 1992; Liedahl et al. 1995) and assumed the abundance ratio among different elements to have solar values. The fits are acceptable for all the ten deprojected shell regions. The deprojected temperature and metallicity profiles thus derived are illustrated in Fig. 2 and Fig. 3, respectively. Compared with the result from the conventional annular spectral analysis, the effect of the projection is clearly seen inside the ~ 60 arcsec radius.

The temperature is consistent with being isothermal in the outskirts beyond ~ 200 kpc, while towards the center it decreases monotonically and reaches 2.8 keV in the innermost shell. Note that the central minimum temperature agrees with the cut-off temperature in a cooling flow model that describes the RGS spectrum (Tamura et al. 2001) and the temperature of the X-ray filament detected with Chandra (Fabian et al. 2001). For usage in the following sections, we obtained an analytical formula that approximates the temperature profile. We employed a formula given as

$$T(R) = T_0 + T_1 \left[1 + \left(\frac{R}{R_{c,T}} \right)^{-\eta} \right]^{-1} \quad (8)$$

which has been proposed by Allen, Schmidt, and Fabian (2001) to give a good description to radial temperature profiles in relaxed clusters. Leaving all the four parameters of T_0 , T_1 , $R_{c,T}$, and η as free parameters, we fitted the temperature profile derived from the deprojected spectra. The parameters obtained from a χ^2 minimization are $T_0 = 2.78^{+0.28}_{-0.38}$ (keV), $T_1 = 3.06^{+0.68}_{-0.45}$ (keV), $R_{c,T} = 50.3^{+10.9}_{-8.6}$ (arcsec), and $\eta = 1.98^{+0.82}_{-0.65}$, where the errors give the 90% confidence range for four parameters of interest ($\Delta\chi^2 = 7.78$). The best-fit function and the error ranges for the individual radii are overlaid in Fig. 2, showing that the function gives a good representation of the temperature profile.

In the metallicity profile (Fig. 3), the strong central concentration of metals found in the previous works (Tamura et al. 2001; Ettori et al. 2002) is confirmed. As for the temperature profile, the metallicity profile was also fitted with a similar function given as

$$A(R) = A_0 + A_1 \left[1 + \left(\frac{R}{R_{c,A}} \right)^2 \right]^{-3/2} . \quad (9)$$

We derived $A_0 = 0.20^{+0.10}_{-0.19}$ (solar), $A_1 = 0.32^{+0.15}_{-0.11}$ (solar), and $R_{c,A} = 149^{+170}_{-82}$ (arcsec), and the best-fit function is overlaid in Fig. 3.

4.4. Mass profile

An immediate way to derive the mass profile is using Eq. (1) with the temperature profile measured in Sect. 4.3 and the density profiles of the ICM which can be obtained from the double β -model profile fitted to the observed X-ray brightness profile in Sect. 4.2. Assuming spherical symmetry, the projected count rate profile in the 0.8-10 keV band, $\Sigma(0.8 - 10\text{keV})$, gives the deprojected radial emissivity profile, $\epsilon(0.8 - 10\text{keV})$, which can be converted to the ICM density via the relation

$$\epsilon(0.8 - 10\text{keV}) = n_g^2 \Lambda(T, A; 0.8 - 10\text{keV}) , \quad (10)$$

where $\Lambda(T, A; 0.8 - 10\text{keV})$ is the emissivity coefficient defined by temperature (T), metallicity (A), energy range (0.8-10 keV), and the instrument responses.

Taking into account the error ranges in the temperature profile, we thus derived the total gravitating mass profile, which is shown in Fig. 4. The result roughly agrees with the mass profile given by Xu et al. (1998) derived from the *ASCA* data with the same method, although a shoulder-like structure found in their profile at ~ 100 kpc is less prominent in our profile. The difference in the mass profiles is mainly attributed to the different parameters of the double β -model profile fitted to the brightness profile.

4.5. Theoretical modeling to the mass profile

The total mass profile thus derived can not be conveniently used in Eq. (3) for determining the dark matter velocity dispersion, however. The term of $d\rho_{\text{DM}}/dR$ in Eq. (3) is calculated from the third derivative of the ICM density profile, i.e. the third derivative of the radial brightness profile which is approximated with the double- β profile, and it gives an uneven profile at the radius where the two β profiles cross over. This causes an unstable behavior in the solution of Eq. (3) and introduces non-negligible systematic errors in the results. Moreover, the double- β modeling on the brightness profile can only reproduce a mass profile with the flat core as long as the temperature profile is virtually flat near the center, and provides rather restrictive mass profile.

Here we make an alternative approach from the derivation above. We start modeling the total mass profile with an analytical formula with a few free parameters that assures a smooth profile with Eq. (3). Combined with the temperature profile derived in Sect. 4.3, the mass profile is used to predict the X-ray surface brightness profile of the cluster to be compared with the data to adjust the free parameters. In the actual calculation, a given total mass profile, $M(< R)$, and a temperature profile, $T(R)$, is converted to the ICM density

profile from Eq. (1) as

$$n_g(R) = n_0 \frac{T(0)}{T(R)} \exp \left[- \int_0^R \frac{G\mu m_p M(< R)}{kT(R)R^2} dR \right], \quad (11)$$

where n_0 is the central ICM density. The emissivity profile in a given energy range, $\epsilon(E_1, E_2)$, is then obtained by Eq. (10), where n_g , T , A are substituted by Eqs. (11), (8) and (9), respectively, which is then converted to the brightness profile, $\Sigma(E_1, E_2)$. Being convolved with the PSF, the model brightness profile is fitted to the 0.8-10 keV count rate profile observed to determine the best-fit parameters in the mass profile model. Although the observational constraint on the ICM temperature profile is limited within 512 arcsec from the center, we apply Eq. (8) beyond the radius, where it describes a practically isothermal model.

As for the mass profile, we apply two representative models having a flat core and a cuspy core. The King model (King 1966) is a classic model for the gravitational potential structure characterized by a flat core. We used an approximated formula of the King model, in which the density profile is given as

$$\rho = \rho_0 \left[1 + \left(\frac{R}{R_c} \right)^2 \right]^{-3/2}, \quad (12)$$

while the integrated mass profile is given as

$$M(< R) = 4\pi R_c^3 \rho_0 \left[\ln \left(\frac{R}{R_c} + \sqrt{\frac{R^2}{R_c^2} + 1} \right) - \frac{R}{R_c} \left(\frac{R^2}{R_c^2} + 1 \right)^{-1/2} \right], \quad (13)$$

where ρ_0 is the central density and R_c is the core radius (see e.g. Binney and Tremaine 1987). The predicted X-ray brightness profile from the King model is fitted to the 0.8-10 keV count rate profile. Fitting parameters are the core radius (R_c) and the central density (ρ_0) of the approximated King model, and the central ICM density (n_0). The best-fit model and the fit residuals are shown in Fig. 5 and the parameters derived are summarized in table 2. The fit is not acceptable. In Fig. 4, the best-fit King model is compared with the mass profile obtained in Sect. 4.4, showing clearly that a central mass excess is necessary in addition to the King model mass.

We then added another King-model component to account for the central mass excess to construct a double approximated King model, which still has a flat core profile. Fitting parameters are now two sets with a core radius and a central density for each ($R_{c,1}$, $\rho_{0,1}$, $R_{c,2}$, and $\rho_{0,2}$), and the central ICM density (n_0). As shown in Fig. 5 and summarized in Table 2, a good fit was obtained.

Another analytical formula for the total mass profile we employed is the universal halo profile by Navarro et al. (1995, 1996, 1997; NFW model), which is characterized by a sharp central cusp. The density profile of the NFW model is given as

$$\rho = \rho_0 \left(\frac{R}{R_s} \right)^{-1} \left[1 + \left(\frac{R}{R_s} \right)^2 \right]^{-2}, \quad (14)$$

where R_s is called scale radius. The integrated mass profile of the NFW model is given as (Makino et al. 1998; Suto et al. 1998)

$$M(< R) = 4\pi\rho_0 R_s^3 \left[\ln \left(1 + \frac{R}{R_s} \right) - \frac{R}{R_s} \left(1 + \frac{R}{R_s} \right)^{-1} \right]. \quad (15)$$

The X-ray count rate profile predicted from the NFW model is fitted to the data, where the free parameters are ρ_0 , R_s , and n_0 . As illustrated in Fig. 5 and summarized in Table 2, the NFW model reproduces the data very well.

For each best-fit mass profiles, the double approximated King model and the NFW model, the corresponding virial mass, M_{vir} , and the virial radius, R_{vir} , are calculated and given in Table 2. The concentration parameters of the NFW model defined as $c \equiv R_s/R_{\text{vir}}$ is obtained to be 6.1. It is worth mentioning that the obtained c and M_{vir} are consistent with the theoretically predicted $c - M_{\text{vir}}$ relation (e.g. Bullock et al. 2001). The double approximated King model and the NFW model obtained above are compared in Fig. 6, together with the mass profile obtained in Sect. 4.4. The three mass profiles are all consistent within the 20-600 arcsec radius region, and they approximately follow $M \propto R^{1.7}$ in this zone. In Fig. 7, the double King model and the NFW model are compared in the mass density profile, together with the corresponding ICM density profile. As clearly seen in Fig. 6 and 7, the two theoretical model profiles differ most significantly in the very central region within ~ 20 arcsec radius, where XMM can not well resolve the spatial structure. Ettori et al. (2002), using Chandra data, obtained the total mass profile in A1795 with finer spatial resolution and found that the density approximately follows $\rho \propto R^{-0.6}$ in the central region. This profile is steeper than the King model ($\rho \propto R^0$) and flatter than the NFW model ($\rho \propto R^{-1}$) near the center. Therefore, the two mass profiles give a conservative mass range. In the next subsection, for determining the dark matter velocity dispersion profile, we use both the double approximated King model and the NFW model for the total mass profile model, which would also be expected to give a conservative range of the velocity dispersion representing systematic uncertainty involved in the usage of a specific mass profile model.

4.6. Dark matter velocity dispersion profile

We now calculate the dark matter velocity dispersion profile by solving the differential equation given in Eq. (3). As the total mass profile, $M(< R)$, the double approximated King model or the NFW model profile obtained in Sect. 4.5 is employed, while the dark matter density profile is obtained from the total mass and the corresponding ICM density profile by $\rho_{\text{DM}}(R) = \frac{1}{4\pi R^2} \frac{dM(< R)}{dR} - \mu m_{\text{p}} n_{\text{g}}(R)$. Both $M(< R)$ and $\rho_{\text{DM}}(R)$ are substituted in Eq. (3) and the differential equation is solved with the fourth-order Runge-Kutta method for various boundary conditions at the center, i.e. $\sigma_{\text{DM}}^2(0)$.

Figure 8 shows a set of solutions of Eq. (3), when the best-fit NFW model is applied to $M(< R)$. Note that there is only a weak observational constraint on the mass profile beyond ~ 1 Mpc and the solution at the large radii depends on the validity of the assumed mass profile. Depending on the inner boundary condition, the dark matter velocity dispersion may fall to zero at small radii, or it may diverge to infinity. In order to select physically plausible solutions among them, we placed a conservative boundary condition that the velocity dispersion at the virial radius is greater than 0 and less than the free fall velocity at this radius.

The constraints on the velocity dispersion profile thus obtained are shown in Fig. 9 individually for different mass models applied. The errors on the ICM temperature profile are properly taken into account to obtain the error bands. In the central region, there is a clear difference between the results from the double approximated King model and the NFW model as expected from their different behavior. The velocity dispersion is then converted to the “temperature” of the dark matter ($kT_{\text{DM}} \equiv \sigma_{\text{DM}}^2 \mu m_{\text{p}}$), which is compared with the ICM temperature in Fig. 10. The ICM temperature is greater than the dark matter “temperature” everywhere. Even in the central region where radiative cooling is expected to be most effective, the ICM temperature is significantly higher than that of the dark matter. The comparison of the temperatures can be more directly described by means of the β_{DM} value defined as $\beta_{\text{DM}} \equiv \sigma_{\text{DM}}^2 \mu m_{\text{p}} / kT = T_{\text{DM}} / T$, which ranges ~ 0.3 - 0.8 (Fig. 11). There is no sign that the ICM is cooled significantly below the dark matter “temperature”. In other words, the dark matter looks to form the temperature floor that limits the ICM temperature.

As a matter of fact, what we derived by solving the Jeans equation is the velocity dispersion of the collisionless particles that includes the dark matter as well as the stellar component. As shown in Fig. 4, the stellar component makes a minor contribution to the total mass and the derived velocity dispersion profile shown in Fig. 10 is virtually that of the dark matter, except in the very central region, where the two components are comparable. If the galaxies alone are in a steady state, they should also obey the Jeans equation under the same gravitational potential. In Fig. 10, we overlay the velocity dispersion profile of

the member galaxies measured by den Hartog and Katgert (1996), and the stellar velocity dispersion of the cD galaxy provided by Blakeslee and Tonry (1992), after converted to “temperature” via $k_{\text{B}}T_* = \mu m_{\text{p}}\sigma_*^2$. They show roughly a consistent profile with that of the dark matter at least in the case when the total mass profile is given by the NFW model.

5. Discussion

5.1. Anisotropy of σ_{DM}

Equation (2) that we have used to calculate the dark matter velocity dispersion profile is based on the assumption of isotropic motion of dark matter particles. However, simulation studies (e.g. Eke, Navarro, and Frenk 1998; Colín, Klypin, & Kravtsov 2000) indicate that the radial velocity dispersion, σ_{r}^2 , should be rather larger than the tangential velocity dispersion, $\sigma_{\text{t}}^2 \equiv \frac{1}{2}(\sigma_{\theta}^2 + \sigma_{\phi}^2)$. The degree of anisotropy is often measured with

$$A \equiv 1 - \frac{\sigma_{\text{t}}^2}{\sigma_{\text{r}}^2}, \quad (16)$$

and the Jeans equation is modified as

$$\frac{GM}{R} = -\sigma_{\text{DM}}^2 \left(\frac{d \ln \rho_{\text{DM}}}{d \ln R} + \frac{d \ln \sigma_{\text{DM}}^2}{d \ln R} + 2A \right). \quad (17)$$

Employing $A = 0.65 \frac{4R/R_{\text{vir}}}{(R/R_{\text{vir}})^2 + 4}$ derived by Colín, Klypin, & Kravtsov (2000), which is as large as 0.5 at the virial radius, R_{vir} , and converging to 0 at the center, we solved Eq. 17 as done in Sect. 4.6. The σ_{DM} profile thus derived for the case of the best fit NFW mass profile is shown in Fig. 12, overlaid with the $A = 0$ solution given in Fig. 9. The σ^2 value with the anisotropy is greater than that without the anisotropy by only $\sim 6\%$ at 100kpc and at most $\sim 40\%$ around 1Mpc.

5.2. Heating source

The β_{DM} profile determined here from observations should provide information on the thermal history of the ICM. From numerical simulation studies, $\beta_{\text{DM}} \sim 1 - 1.4$ is expected, if there is no cooling or additional heating (e.g. Metzler and Evrard 1994; Navarro et al. 1995; Bryan & Norman 1998). An obvious way to explain the β_{DM} value smaller than unity in A1795 is heating of the ICM.

As suggested from the break of the self-similarity between dark matter and ICM, there should have been non-gravitational heating acting globally. We, from our results, estimated the excess energy of the ICM over that of the dark matter particles as

$$\Delta E(< R) = \frac{3}{2} (< kT > - \mu m_p < \sigma_{\text{DM}}^2 >) , \quad (18)$$

where $\langle \rangle$ denotes mass weighted mean within radius, R . As shown in fig. 13, the excess energy, ΔE , thus derived is found to be $\sim 1 - 3$ keV per particle, which may be compared with theoretical model predictions. The amount of energy injection to the gas phase that explains e.g. the observed $L - T$ relation depends on the period when the heating occurred. Heating prior to cluster collapse, “preheating”, needs $0.1 - 0.3$ keV per particle (e.g. Navarro et al. 1995; Tozzi & Norman 2001), while heating after a cluster formation requires higher values of $1 - 3$ keV per particle (e.g. Metzler & Evrard 1994; Loewenstein 2000; Wu, Fabian, & Nulsen 2000; Bower et al. 2001). Our results given above may indicate that the global non-gravitational heating that may cause the break of self similarity has happened mainly within a collapsed cluster. However, even if such non-gravitational heating that explains the global X-ray feature of the cluster is provided, the central region of A1795 has a short radiative cooling time (Fig. 14), and there must be another significant energy input to the ICM in the central region at the present epoch to prevent the ICM from cooling.

As a possible energy source in the central region, we first consider gravitational energy of the member galaxies and stellar components therein. The kinetic energy of the random motion of stars can be partially transferred to the ICM by stellar mass loss. Gas supplied by stellar mass loss has velocities of the bulk motions of stars relative to the ICM, which is the sum of a galaxy motion and the motions of the stars in the galaxy, and is likely to be thermalized by interactions with the ambient gas. If the stellar component moving in the same gravitational potential has a similar velocity dispersion profile as that of the dark matter (Fig. 10), the gas temperature achieved from this process is expected to be comparable to the velocity dispersion of the dark matter. This process nicely accounts for X-ray emission from isolated X-ray compact elliptical galaxies (Matsushita 2001). The input rate of the kinetic energy of the gas from stellar mass loss may be simply estimated as $\dot{E} = 1/2 M_{\text{star}} \dot{m} \sigma^2 = 10^{42}$ ergs/s, where M_{star} is the total stellar mass of $1 \times 10^{12} M_{\odot}$, $\dot{m} = 3 \times 10^{11} M_{\odot} \text{ yr}^{-1}$ ($10^{11} M_{\odot}$) $^{-1}$ is the stellar mass loss rate in unit time, and $\sigma (= 580 \pm 80 \text{ km/s})$ is the velocity dispersion of the galaxies from den Hartog & Katgert (1996; Fig. 10). (The stellar velocity dispersions in the galaxies are smaller and neglected here.) This is much smaller than the output energy in the central region by X-ray radiation in galaxy clusters like A1795, however. Thus for the case of galaxy clusters, we have to look for additional heat sources.

Kinetic energy of the stellar component might be more efficiently transferred to ICM via magnetic fields. As pointed out by e.g. Makishima et al. (2001), the motion of stars

may amplify interstellar magnetic fields and reconnections of the fields may heat up the ICM rather efficiently. The galaxies must have lost their kinetic energies through interactions with the ICM and have gradually fallen inwards accumulating onto the central galaxy to form the cD galaxy. A deep optical image of the cD galaxy in A1795 derived by Johnstone et al. (1991) shows a concentration of elliptical galaxies of various sizes and stars forming a largely extended envelope with $131 h_{70}^{-1}$ kpc effective radius, which strongly suggests the on-going formation process of the cD galaxy. Quantitatively, the total amount of dynamical energy of the stellar component in the member galaxies that has been lost in the past is estimated. The stellar component in the galaxies is assumed to have a negligible small potential (U) and kinetic energy (K) before the formation of the cluster, and the current energy of the stars is estimated to be $U + K \sim -10^{62}$ ergs. If the energy has been released over the last 10 Gyr and has been spent in ICM heating, the heating luminosity is expected to be $\sim 3 \times 10^{44}$ ergs s^{-1} . This amounts to the bolometric luminosity of the ICM within $60h_{70}^{-1}$ kpc (Fig. 14), and may be sufficient to sustain the thermal energy of the ICM against radiative cooling. This model predicts that the stellar velocity dispersion became smaller than that of ICM, i.e. $\beta_{\text{spec}} < 1$, which is consistent with the actual observed value in the central region (Fig. 10).

Alternatively, there may be sufficient non-gravitational heat input from an active galactic nucleus (AGN) powered by an accretion of low entropy gas at a cluster center (Churazov et al. 2002; Böhringer et al. 2002). Numerical simulations show that an outflow from an AGN may form hot bubbles of relativistic plasma rising with buoyancy, and the bubbles may uplift cold gas mixing with ambient ICM (Churazov et al. 2001; Quilis, Bower, & Balogh 2001; Brüggén & Kaiser 2002; Basson & Alexander 2003). High resolution imaging observations revealed ripples and shock features in the central region of Perseus cluster (Fabian et al. 2003) and M87 (Forman et al. 2004), suggesting that the bubble energy may also be transferred by sound wave to larger distances, and that shocks may be the major contribution of the energy dissipation. The heating mechanism is self regulated: the lower the entropy, the higher the accretion rate onto the central engine. A portion of the accretion power is dissipated back into the ICM to make its entropy high and regulate the accretion rate to achieve an equilibrium state. This process automatically prevents the persistence of cold and hence dense clouds. The cD galaxy of A1795 has a radio source, 4C26.42, and the existence of an AGN is evident. Using the physical state of the ICM in the center we can actually estimate the energy provided by the AGN by applying the Bondi accretion model. According to the well-known correlation of the black hole mass with the mass of the bulge component (Magorrian et al. 1998), the black hole mass is expected to be $\sim 6 \times 10^9 M_{\odot}$. Assuming that the gas profile is flat in the center, we can use the measured values of $n_g=0.1$

cm^{-3} and $T_0=2.8$ keV to obtain the Bondi mass accretion rate

$$\dot{M} = 4\pi 0.25 \rho_\infty c_{s,\infty}^{-3} (GM_{\text{BH}})^2 \quad (19)$$

$$= 0.23 M_\odot/\text{yr} \left(\frac{n}{1\text{cm}^{-3}} \right) \left(\frac{T}{1\text{keV}} \right)^{-3/2} \left(\frac{M_{\text{BH}}}{6 \times 10^9 M_\odot} \right)^2, \quad (20)$$

where ρ_∞ and $c_{s,\infty}$ are the density and sound velocity outside the Bondi accretion radius. We find $\dot{M} \sim 0.4 \times 10^{-2} M_\odot/\text{yr}$. Under the standard assumption of 10% of the accretion energy to be dissipated, the output energy is found to be $E = 0.1 \dot{M} c^2 \sim 3 \times 10^{43}$ ergs/s. This amounts to the X-ray luminosity within the inner ~ 20 kpc region only. The Bondi accretion radius is estimated to be $R_B \sim GM_{\text{BH}}/c_s^2 \sim 30$ pc, much smaller than the resolution of the temperature and density structure that can be measured with XMM-Newton. If the ICM density is not uniform but is clumpy, the Bondi accretion rate should be significantly larger and the heating rate could also be larger than the above estimation. We can note that the ICM conditions might temporally vary and that we currently see a relatively low state.

Note that there are other heating mechanisms discussed, which include e.g. a classical idea of thermal conduction from the hot outer regions (e.g. Takahara & Takahara 1979; Tucker & Rosner 1983; Bregman, & David 1988; Gaetz 1989), and the acoustic wave heating recently proposed by Fujita, Suzuki, & Wada (2004). Comparison of those model predictions with our results presented in the current paper would be very interesting.

6. Summary

We derived the dark matter velocity dispersion profile from an X-ray observation for the first time. Using the XMM-Newton EPIC data of A1795, we derived β_{DM} of $\sim 0.3 - 0.8$, indicating that the ICM temperature is larger than the dark matter “temperature” everywhere. We also derived the excess energy in the ICM, ΔE , which is found to be $\sim 1 - 3$ keV per particle. These observational quantity should be useful to provide a new clue to solve the heating mechanism in the cooling core and to understand the thermal history of a galaxy cluster.

We thank the XMM team for providing the data and the data analysis tools. In particular, we express our gratitude to Michael Freyberg for helping the data analysis. We also acknowledge FTOOLS. We thank Kuniaki Masai for helpful discussions. We are also grateful to Paul Lynam for critically reading this manuscript.

REFERENCES

- Allen, S. W., Fabian, A. C., Johnstone, R. M., Arnaud, K. A. & Nulsen, P. E. J. 2001, MNRAS, 322, 589
- Allen, S. W., Schmidt, R. W., & Fabian, A. C. 2001, MNRAS, 328, L37
- Allen, S. W. & Fabian, A. C. 1994, MNRAS, 269, 409
- Arnaud, M., Neumann, D. M., Aghanim, N., Gastaud, R., Majerowicz, S., & Hughes, J. P. 2001, A&A, 365, L80
- Basson, J. F., & Alexander, P. 2003, MNRAS, 339, 353
- Binney, J., & Tremaine, S. 1987, GALACTIC DYNAMICS, Princeton University Press
- Blakeslee, J. P., & Tonry, J. L. 1992, AJ, 103, 1457
- Böhringer, H., Briel, U. G., Schwarz, R. A., Voges, W., Hartner, G. & Trumper, J. 1994, Nature, 368, 828
- Böhringer, H., Matsushita, K., Churazov, E., Ikebe, Y., & Chen, Y. 2002, A&A, 382, 804
- Boute, D. A., & Tsai, J. C. 1996, ApJ, 458, 27
- Bower, R. G., Benson, A. J., Lacey, C. G., Baugh, C. M., Cole, S., & Frenk, C. S. 2001, MNRAS, 325, 497
- Bregman, J. N., & David, L. P. 1988, ApJ, 326, 639
- Briel, U. G., & Henry, J. P. 1996, ApJ, 472, 131
- Brüggen, M., & Kaiser, C. R. 2002, Nature, 418, 301
- Bryan, G. L. & Norman, M. L. 1998, ApJ, 495, 80
- Bullock, J. S., Kolatt, T. S., Sigad, Y., Somerville, R. S., Kravtsov, A. V., Klypin, A. A., Primack, J. R., & Dekel, A. 2001, MNRAS, 321, 559
- Burkert, A. 1995, ApJ, 447, L25
- Canizares, C. R., Stewart, G. C., & Fabian, A. C. 1983, ApJ, 272, 449
- Churazov, E., Brüggen, M., Kaiser, C. R., Böhringer, H., & Forman, W. 2001, ApJ, 554, 261

- Churazov, E., Sunyaev, R., Forman, W., Böhringer, H. 2002, MNRAS, 332, 729
- Colín, P., Klypin, A. A., Kravtsov, A. V. 2000, ApJ, 539, 561
- Cowie, L. L., & Binney, J. 1977, ApJ, 215, 723
- David, L. P., Slyz, A., Jones, C., Forman, W., Vrtillek, S. D., & Arnaud, K. A. 1993, ApJ, 412, 479
- David, L. P., Jones, C., Forman, W. & Daines, S. 1994, ApJ, 428, 544
- den Hartog, R., & Katgert, P. 1996, MNRAS, 279, 349
- Edge, A. C., & Stewart, G. C. 1991, MNRAS, 252, 414
- Edge, A. C., Stewart, G. C., & Fabian, A. C. 1992, MNRAS, 258, 177
- Eke, Navarro, & Frenk (1998), ApJ, 503, 569
- Ettori, S., Fabian, A. C., Allen, S. W., & Johnstone, R. M. 2002, MNRAS, 331, 635
- Fabian, A. C., Hu, E. M., Cowie, L. L., & Grindlay, J. 1981, ApJ, 248, 47
- Fabian, A. C., Nulsen, P. E. J., & Canizares, C. R. 1984, Nature, 310, 733
- Fabian, A. C. 1994, ARA&A, 32, 277
- Fabian, A. C., Arnaud, K. A., Bautz, M. W., & Tawara, Y. 1994, ApJ, 436, L63
- Fabian, A. C., Mushotzky, R. F., Nulsen, P. E. J., & Peterson, J. R. 2001a, MNRAS, 321, L20
- Fabian, A. C., Sanders, J. S., Ettori, S., Taylor, G. B., Allen, S. W., Crawford, C. S., Iwasawa, K., & Johnstone, R. M. 2001b, MNRAS, 321, L33
- Fabian, A. C., Sanders, J. S., Allen, S. W., Crawford, C. S., Iwasawa, K., Johnstone, R. M., Schmidt, R. W., and Taylor, G. B. 2003, MNRAS, 344, L43
- Forman, W. et al. astro-ph/0312576
- Fujita, Y., Suzuki, T. K., & Wada, K. 2004, ApJ, 600, 650
- Fukushige, T., & Makino, J. 2001, ApJ, 557, 533
- Gaetz, T. J. 1989, ApJ, 345, 666

- Ghizzardi, S 2001, XMM-SOC-CAL-TN-0022, <http://xmm.vilspa.esa.es/docs/documents/CAL-TN-0022-1-0.ps.gz>
- Hughes, J. P. 1989, *ApJ*, 337, 21
- Ikebe, Y., Makishima, K., Fukazawa, Y., Tamura, T., Xu, H., Ohashi, T., & Matsushita, K. 1999, *ApJ*, 525, 58
- Johnstone, R. M., Naylor, T., & Fabian, A. C. 1991, *MNRAS*, 248, 18p
- Jones, C., & Forman, W. 1984, *ApJ*, 276, 38
- Kaastra, J.S. 1992, An X-Ray Spectral Code for Optically Thin Plasmas (Internal SRON-Leiden Report, updated version 2.0)
- Kaastra, J. S., Ferrigno, C., Tamura, T., Paerels, F. B. S., Peterson, J. R., & Mittaz, J. P. D. 2001, *A&A*, 365, L99
- Kaiser, N. 1986, *MNRAS*, 222, 323
- Kitayama, T., & Suto, Y. 1996, *ApJ*, 469, 480
- King, I. R. 1966, *AJ*, 71, 276
- Liedahl, D. A., Osterheld, A. L. & Goldstein, W. H. 1995, *ApJ*, 438, L115
- Loewenstein, M. 2000, *ApJ*, 532, 12
- Magorrian, J., Tremaine, S., Richstone, D., Bender, R., Bower, G., Dressler, A., Faber, S. M., Gebhardt, K., Green, R., Grillmair, C., Kormendy, J., & Lauer, T. 1998, *AJ*, 115, 2285
- Makino, N., Sasaki, S., & Suto, Y. 1998, *ApJ*, 497, 555
- Makishima, K. et al. 2001, *PASJ*, 53, 401
- Matsushita, K. *ApJ*, 547, 693
- Metzler, C. A., & Evrard, A. E. 1994, *ApJ*, 437, 564
- Mewe, R., Gronenschild, E. H. B. M., & van den Oord, G. H. J. 1985, *A&AS*, 62, 197
- Mewe, R., Lemen, J. R., & van den Oord, G. H. J. 1986, *A&AS*, 65, 511
- Moore, B., Quinn, T., Governato, F., Stadel, J., Lake, G. et al. 1999, *MNRAS*, 310, 1147

- Navarro, J. F., Frenk, C. S., & White, S. D. W. 1995, MNRAS, 275, 720
- Navarro, J. F., Frenk, C. S., & White, S. D. M. 1996, ApJ, 462, 563
- Navarro, J. F., Frenk, C. S., & White, S. D. M. 1997, ApJ, 490, 493
- Peterson, J. R. et al. 2001, A&A, 365, L104
- Ponman, T. J., Cannon, D. B., & Navarro, J. F. 1999, Nature, 397, 135
- Quilis, V., Bower, R. G., & Balogh, M. L. 2001, MNRAS, 328, 1091
- Suto, Y., Sasaki, S., & Makino, N. 1998, ApJ, 509, 544
- Struble, M. F., & Rood, H. J. 1987, ApJS, 63, 543
- Strüder et al. 2001, A&A, 365, 18L
- Tamura, T. et al. 2001, A&A, 365, L87
- Takahara, M., & Takahara, F. 1979, Prog. Theor. Phys., 62, 1253
- Tozzi, P., & Norman, C. 2001, ApJ, 546, 63
- Tucker, W. H., & Rosner, R. 1983, ApJ, 267, 547
- White, D. A., Jones, C., & Forman, W. 1997, MNRAS, 292, 419
- Wu, K. K. S., Fabian, A. C., & Nulsen, P. E. J. 2001, MNRAS, 318, 889
- Wu, X., Xue, Y., & Fang, L. 1999, ApJ, 524, 22
- Xu, H., Makishima, K., Fukazawa, Y., Ikebe, Y., Kikuchi, K., Ohashi, T., & Tamura, T.
1998, ApJ, 500, 738

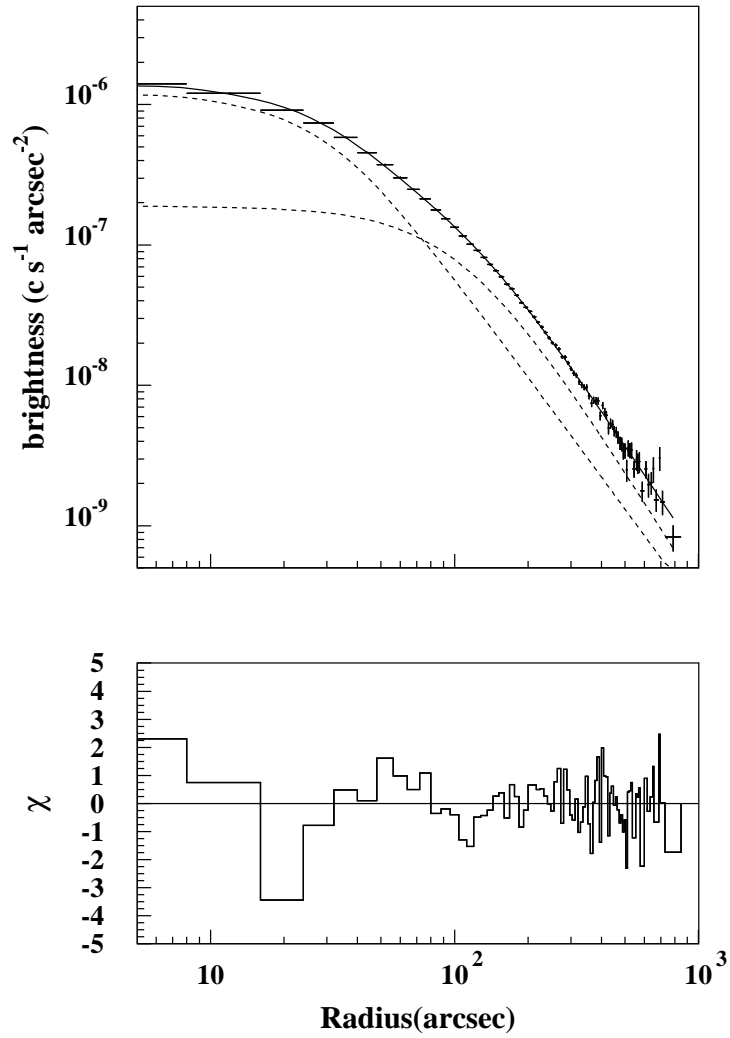


Fig. 1.— In the upper panel, the 0.8–10 keV X-ray count rate profile shown in crosses is fitted with a double β -model (solid line). The dotted lines show the individual β -model components. The fit residuals are shown in the lower panel.

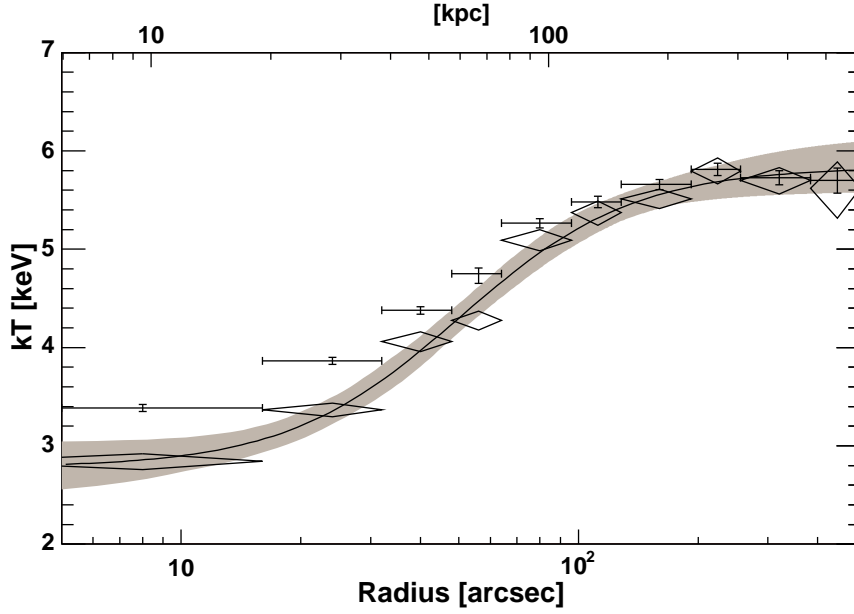


Fig. 2.— The ICM temperature profile of A1795 derived from the spectral analysis with the XMM-Newton EPIC-MOS and EPIC-PN data. Results from the deprojected spectra are shown with diamonds, while the conventional annular spectral analysis gives the profile with crosses. The solid line shows the best-fit function given as $T(R) = 2.78 + 3.06 \left[1 + \left(\frac{R(\text{arcsec})}{50.3} \right)^{-1.98} \right]^{-1}$ (keV), while the gray hatched region shows 90% error region with the function.

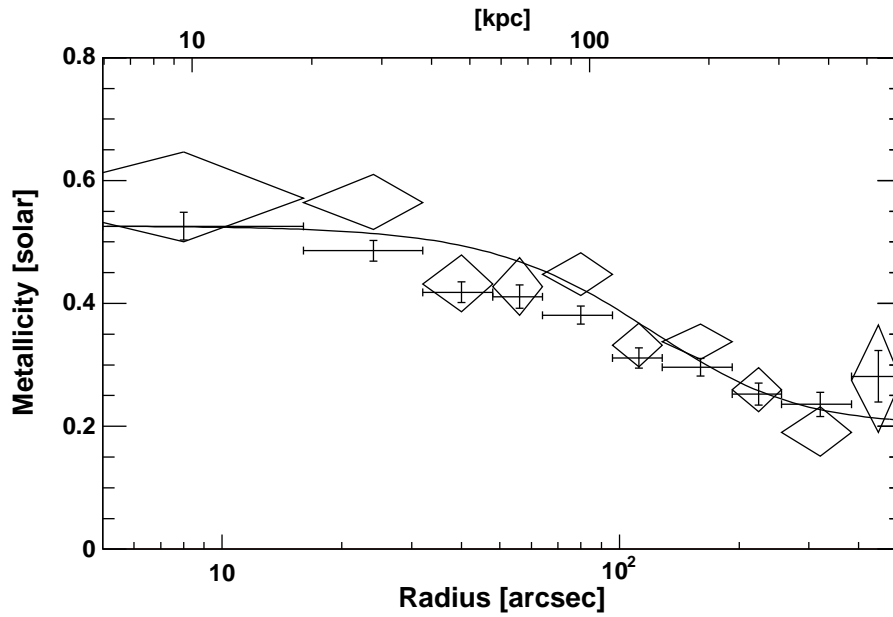


Fig. 3.— The metallicity profile of A1795. Results from the deprojected spectra are shown with diamonds, while the conventional annular spectral analysis gives the profile with crosses. The solid line shows the best-fit function given as $A(R) = 0.20 + 0.32(1 + (R/149)^2)^{-1.5}$.

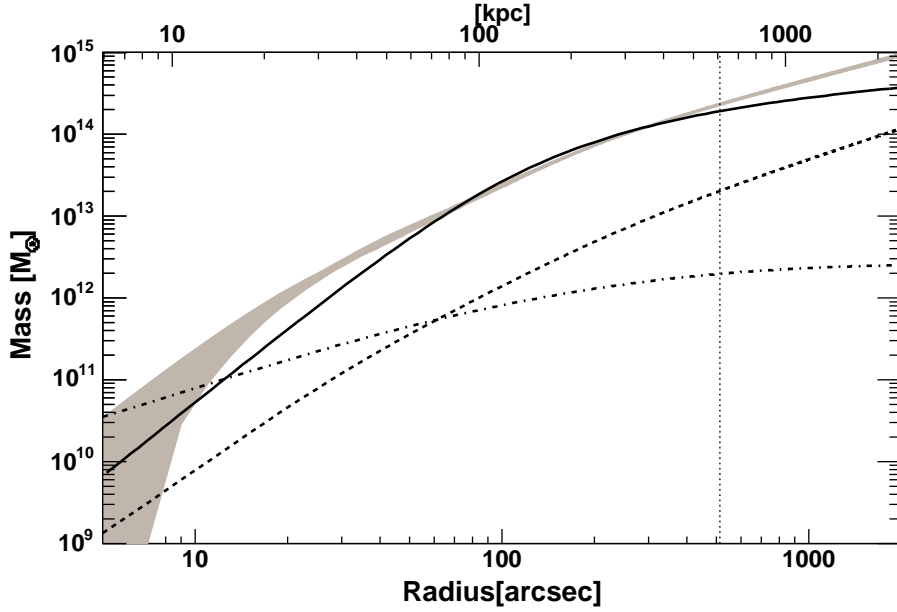


Fig. 4.— The grey hatched region illustrates the integrated radial profile of the total gravitating mass obtained via Eq. (1). The errors in the ICM temperature profile illustrated in Fig. 2 is properly propagated to obtain the error range at the individual radii. The vertical dotted line indicates the radius within which the ICM temperature measurements are available, and isothermality is assumed beyond the radius. The dashed line shows the ICM mass profile calculated from integrating the ICM density profile, where the errors are smaller than the line width. The dot-dashed line shows the stellar mass profile, estimated from an *I*-band image obtained by Johnstone et al. (1991). We approximated the *I*-band surface brightness profile with a de Vaucouleurs law given as $\mu[\text{mag arcsec}^{-2}] = 25.0 + 8.33 \left[\left\{ \frac{r(\text{arcsec})}{150} \right\}^{1/4} - 1 \right]$, and converted it to the mass profile assuming $B-I=2.28$ and a mass-to-light ratio of 6.5 in *B*-band. The solid line indicates an approximated King profile (Eq. 12 and 13) derived by fitting it to the data via Eqs. (10) and (11).

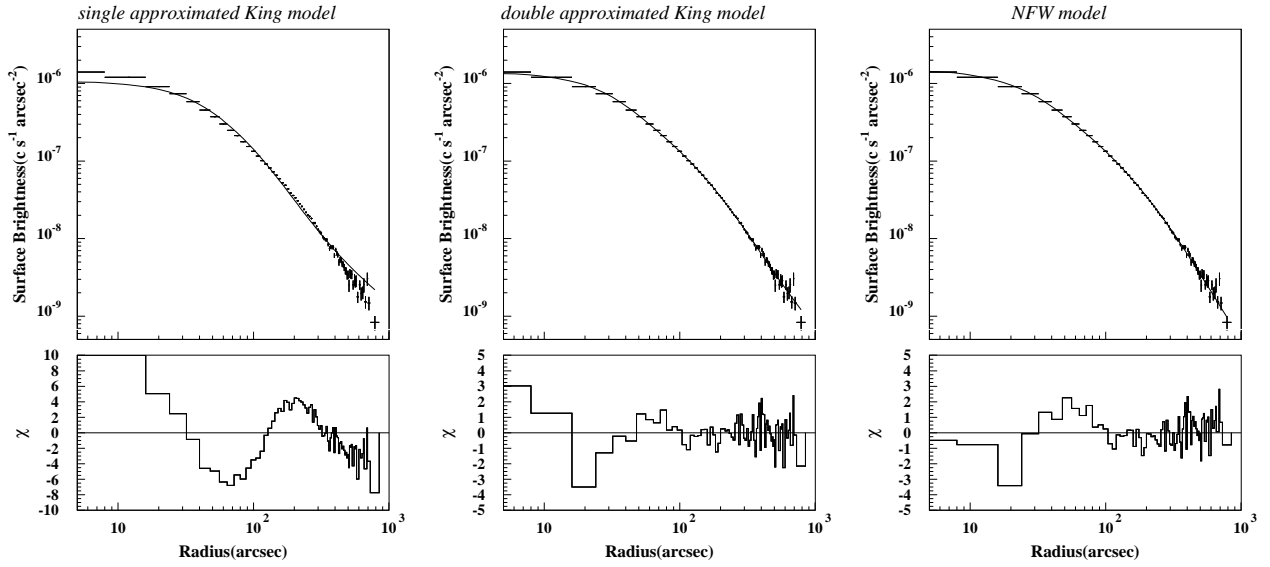


Fig. 5.— The upper panels show the 0.8–10 keV X-ray count rate profile (crosses) and the best-fit model profiles predicted from given total mass profiles. The mass profile assumed in the model for the left, middle and right panel is single approximated King model, double approximated King model and NFW model, respectively. The lower panels show residuals for the best-fit model profiles.

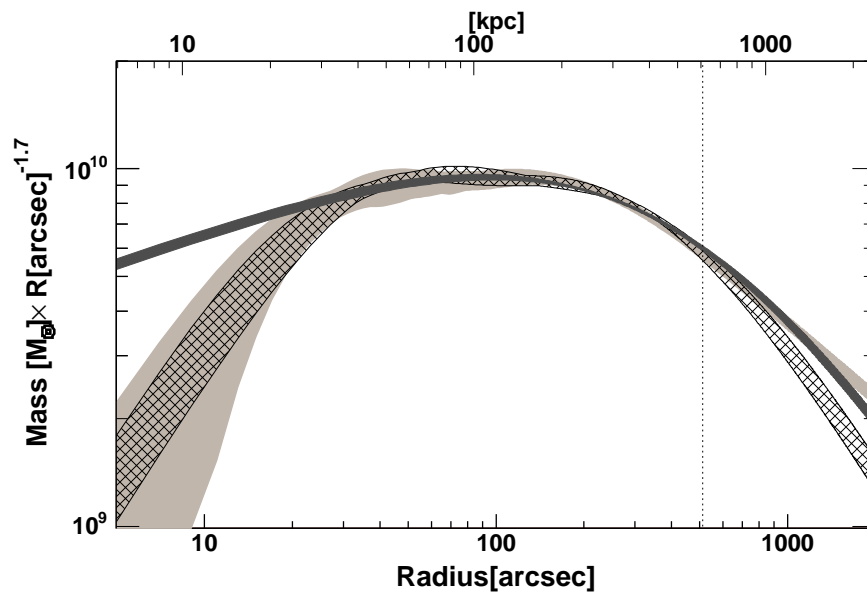


Fig. 6.— The scaled total mass profiles obtained in Sect. 4.4 (light gray band) and the two theoretical models, the double approximated King model (hatched region with oblique lines) and the NFW model (dark gray band) obtained in Sect. 4.5 are compared. The vertical axis shows the integrated mass multiplied by $R^{-1.7}$. The vertical dotted line is the same as in Fig. 4.

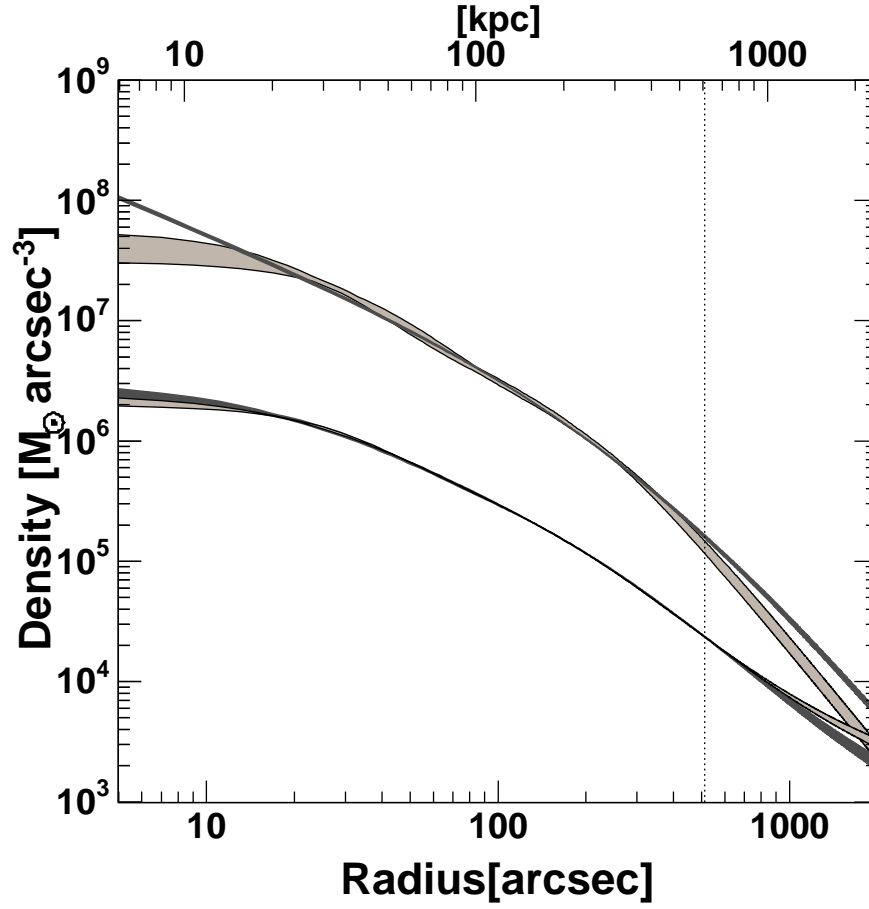


Fig. 7.— The upper curves show the mass density profiles of the total gravitating matter, while the lower curves show the ICM density profiles. The results with the double approximated King model and those with the NFW model are illustrated with light gray band and dark gray band, respectively. The vertical dotted line is the same as in Fig. 4.

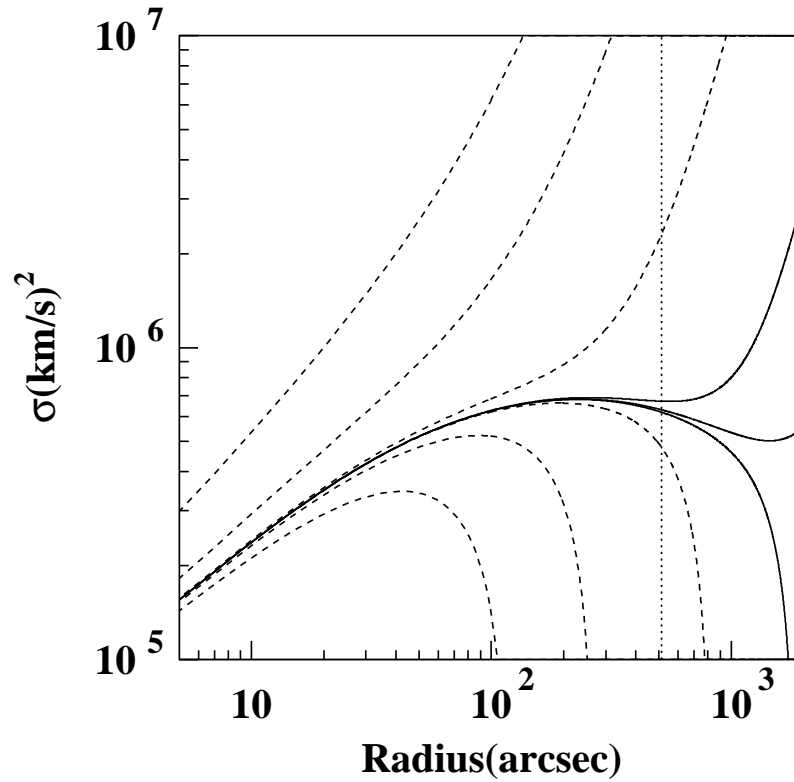


Fig. 8.— Solutions of Eq. (3) with different $\sigma_{\text{DM}}(0)$ values, when the best-fit NFW model is used for the mass profile. Physically plausible solutions are illustrated in the solid lines, while the dashed lines are other possible solutions. The vertical dotted line is the same as in Fig. 4.

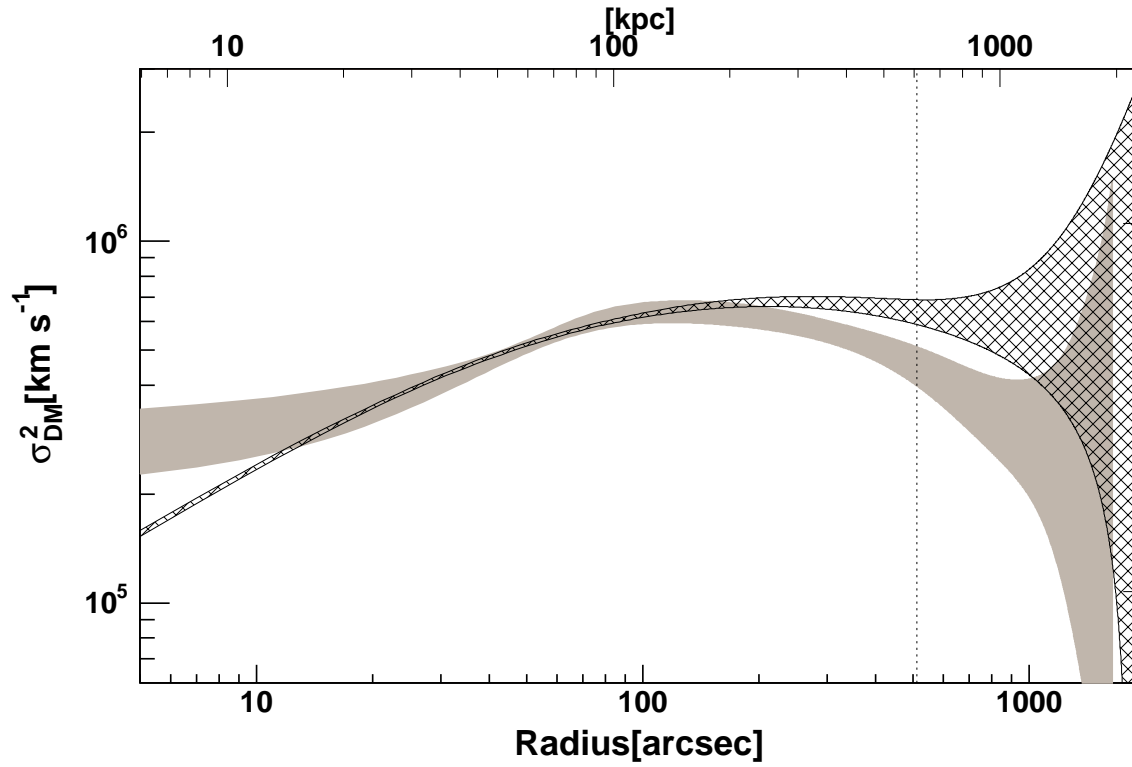


Fig. 9.— The velocity dispersion profiles of the dark matter are shown with the error bands. The gray hatched region and the hatched region with oblique lines are derived from the double approximated King model and the NFW model as the total mass profile, respectively. The vertical dotted line is the same as in Fig. 4.

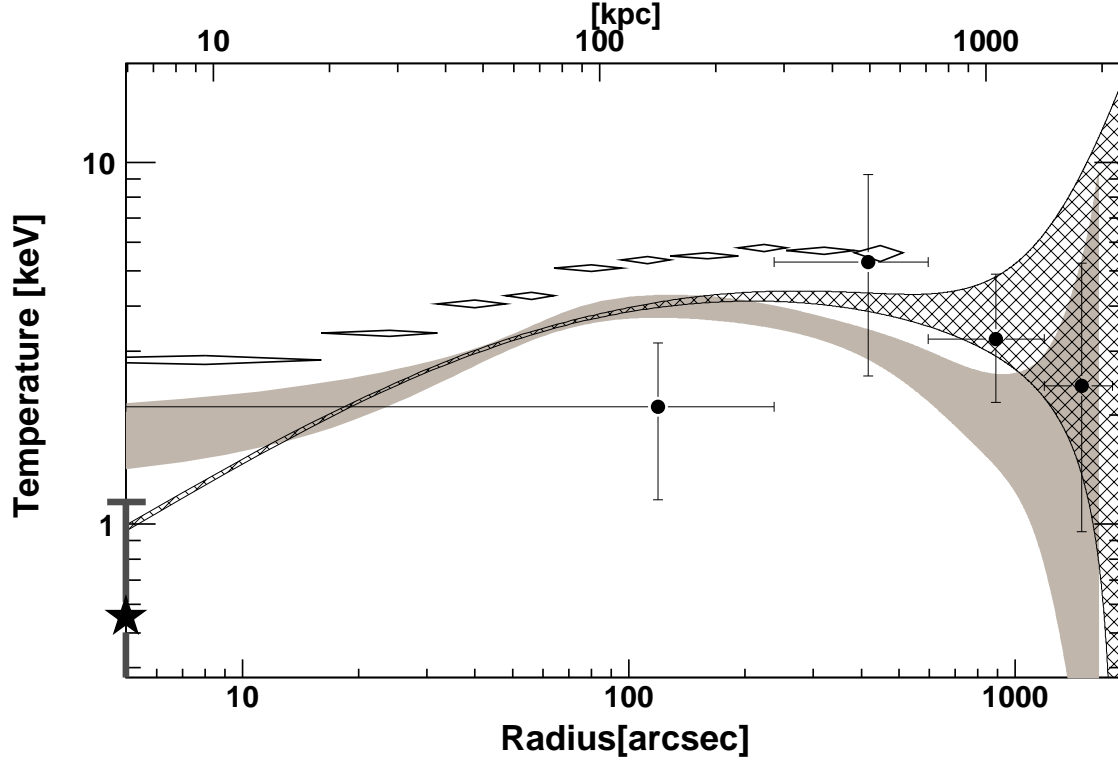


Fig. 10.— The velocity dispersion profiles shown in Fig. 9 are converted to “temperature” via $kT_{\text{DM}} = \mu m_{\text{p}} \sigma_{\text{DM}}^2$. The ICM temperature profile derived in Sect. 4.3 and shown in Fig. 2 is overlaid with diamonds. “Temperatures” of member galaxies derived by $\mu m_{\text{p}} \sigma_{\text{gal}}^2$ are also indicated with crosses, where the galaxy velocity dispersions (σ_{gal}) are taken from observations by den Hartog & Katgert (1996). The star symbol with the gray vertical error bar indicates the central stellar velocity dispersion of the cD galaxy being converted to “temperature” by $\mu m_{\text{p}} \sigma_{\text{stellar}}^2$, where we use $\sigma_{\text{stellar}} = 297 \pm 12$ (km s^{-1}) as measured by Blakeslee & Tonry (1992).

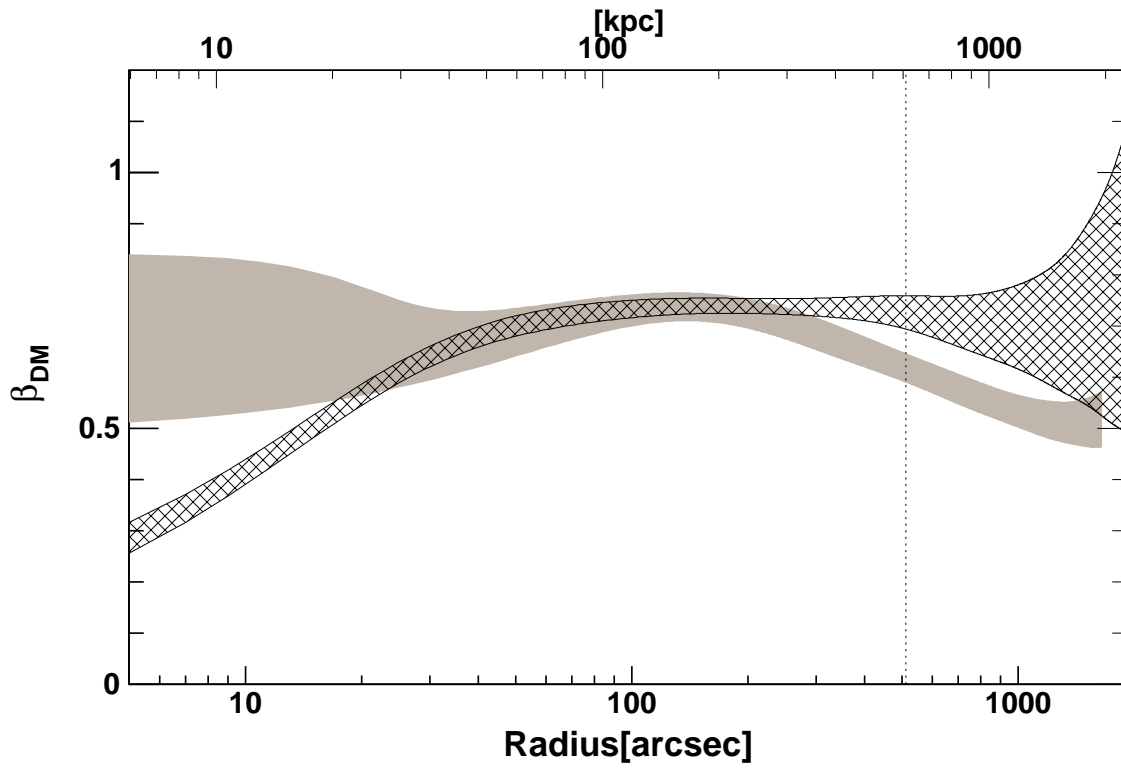


Fig. 11.— Radial profile of β_{DM} . The gray region and the hatched region with oblique lines correspond to the solutions shown in Fig. 9. The vertical dotted line is the same as in Fig. 4.

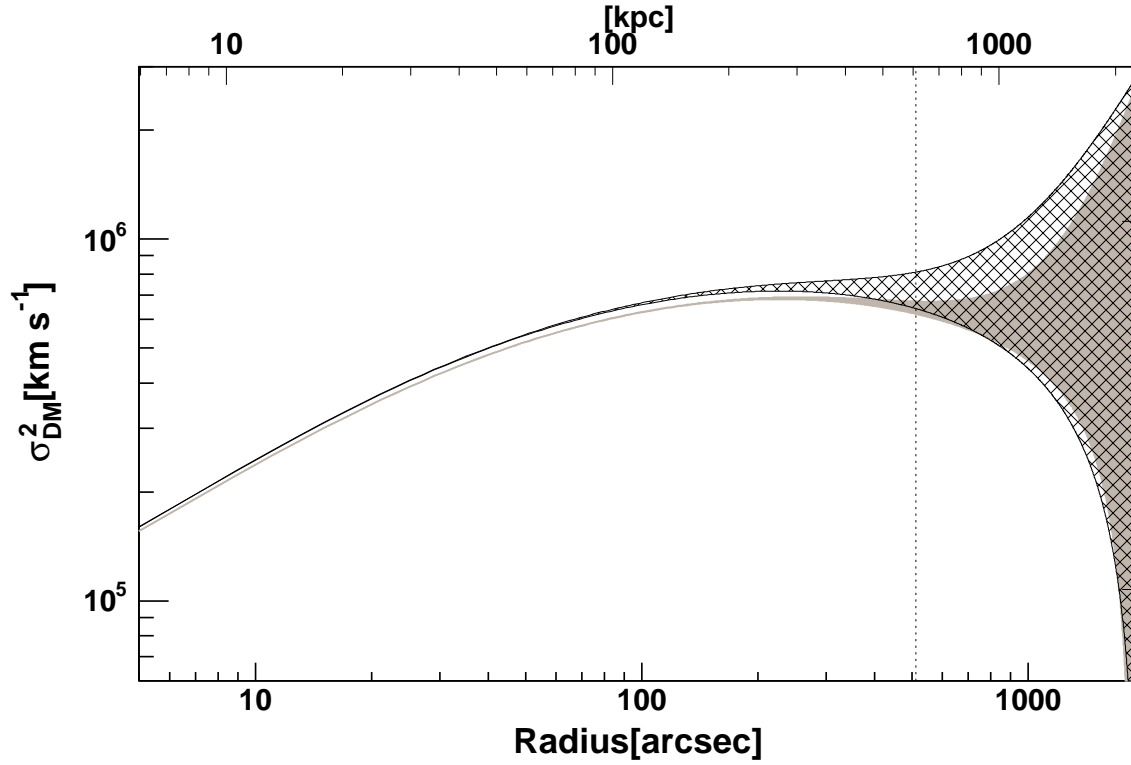


Fig. 12.— The hatched region with oblique lines shows the velocity dispersion profile of the dark matter, when the NFW model is used as the total mass profile and the anisotropy of the velocity distribution is introduced as $A = 0.65 \frac{4R/R_{\text{vir}}}{(R/R_{\text{vir}})^2 + 4}$. The solution in the isotropic case is overlaid with the gray hatched region. The vertical dotted line is the same as in Fig. 4.

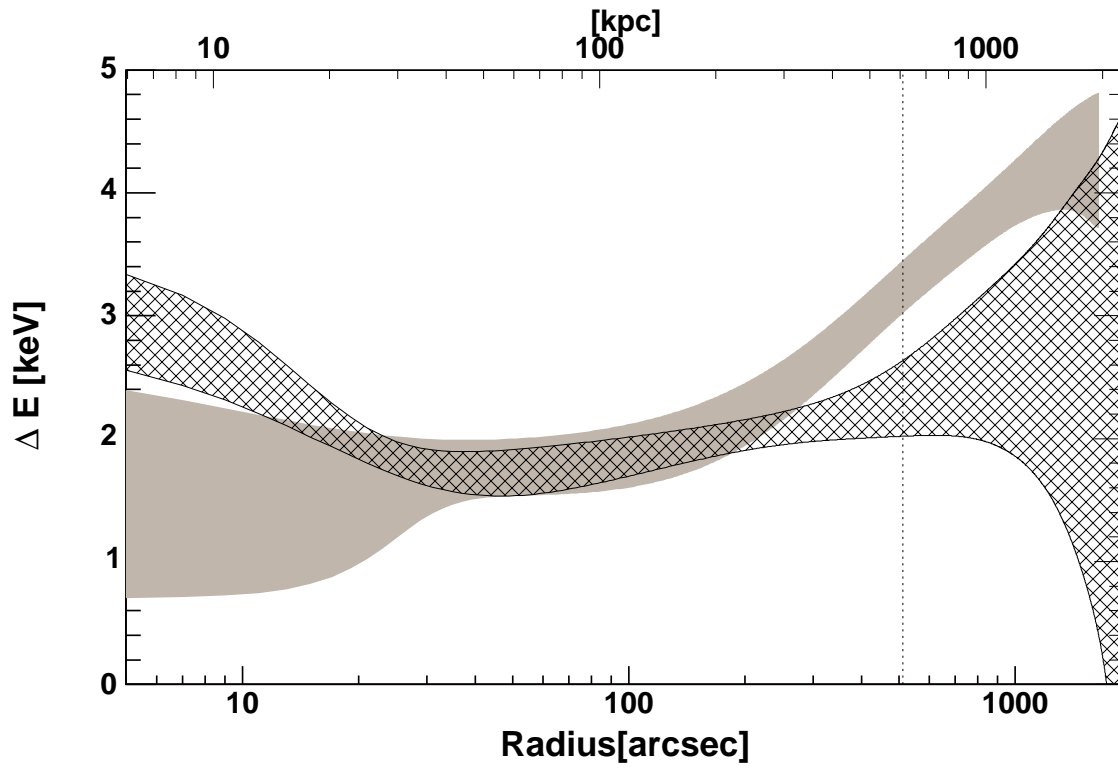


Fig. 13.— Radial profile of ΔE . The gray region and the hatched region with oblique lines correspond to the solutions shown in Fig. 9. The vertical dotted line is the same as in Fig. 4.

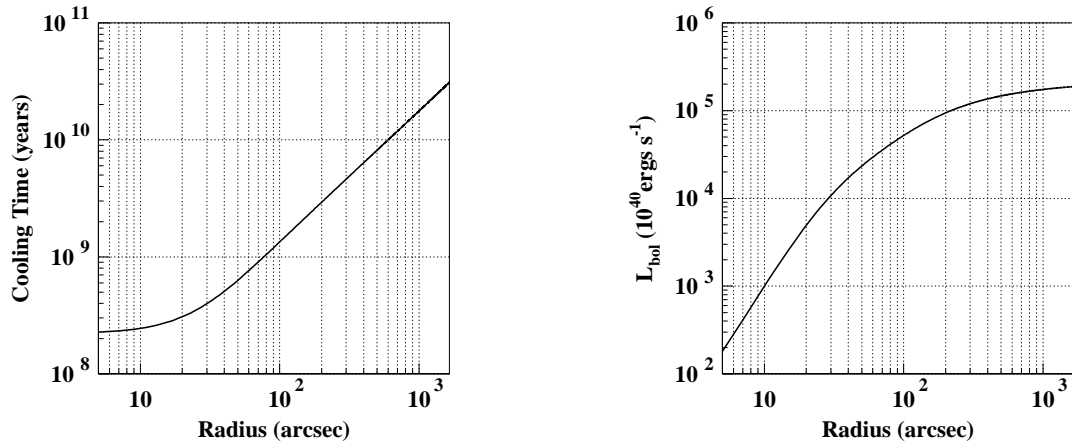


Fig. 14.— (Left panel) Radiative cooling time of the ICM calculated from the density and temperature at each radius. (Right panel) Bolometric luminosity integrated within each radius.

Table 1. Best-fit parameters of the double β model fitted to the 0.8-10 keV brightness profile

parameter	value ^{a)}	
$\Sigma_{0,1}$	$(1.42 \pm 0.04) \times 10^{-6}$	[c/s/arcsec ²]
$R_{c,1}$	26.3 ± 1.0	[arcsec]
β_1	0.562 ± 0.015	
$\Sigma_{0,2}$	$(1.92 \pm 0.12) \times 10^{-7}$	[c/s/arcsec ²]
$R_{c,2}$	106 ± 4	[arcsec]
β_2	0.633 ± 0.010	
χ^2/ν	83.2/74	

^aErrors are 90% ($\Delta\chi^2 = 2.7$) confidence.

Table 2.

mass model	$\rho_{0,1}$ [$M_{\odot}\text{arcsec}^{-3}$]	$R_{c,1}$ [arcsec]	$\rho_{0,2}$ [$M_{\odot}\text{arcsec}^{-3}$]	$R_{c,2}$ [arcsec]	$n_g(0)$ [cm^{-3}]	χ^2/ν	$R_{\text{vir}}^a)$ [arcsec (Mpc)]	$M_{\text{vir}}^a)$ [$10^{14}M_{\odot}$]
1 King	1.28×10^7	94.6	–	–	0.063	1124/77	–	–
2 King	$3.31^{+1.76}_{-0.42} \times 10^7$	$34.8^{+6.9}_{-10.9}$	$2.74^{+1.54}_{-0.79} \times 10^6$	$194.4^{+26.4}_{-34.7}$	$0.086^{+0.014}_{-0.006}$	88.3/75	1716^{+63}_{-74} ($2.04^{+0.07}_{-0.09}$)	$5.38^{+0.62}_{-0.66}$
NFW	$1.64^{+0.18}_{-0.13} \times 10^6$	$330.2^{+16.1}_{-21.9}$	–	–	$0.118^{+0.022}_{-0.012}$	88.7/77	1958^{+26}_{-44} ($2.33^{+0.03}_{-0.06}$)	$8.01^{+0.32}_{-0.54}$

^a $M_{\text{vir}} \equiv \frac{4}{3}\pi R_{\text{vir}}^3 \rho_0 (1+z)^3 \Delta$, where ρ_0 is the mean density of the universe at present, and Δ is the ratio between a cluster mean density and the mean density of the universe at the cluster-formation redshift z ($=0.0616$ for A1795) (see e.g. Kitayama & Suto 1996).